Journal of Molecular Liquids 337 (2021) 116578

Contents lists available at ScienceDirect

Journal of Molecular Liquids

journal homepage: www.elsevier.com/locate/molliq

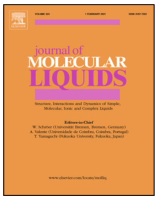

Fabrication of magnetic cerium-organic framework-activated carbon composite for charged dye removal from aqueous solutions

Roxana Paz [a], Herlys Viltres [a,*], Nishesh Kumar Gupta [b,c], Carolina Leyva [a,*]

[a] *Instituto Politécnico Nacional, Centro de Investigación en Ciencia Aplicada y Tecnología Avanzada, CDMX, Mexico*
[b] *University of Science and Technology (UST), Daejeon, Republic of Korea*
[c] *Department of Land, Water, and Environment Research, Korea Institute of Civil Engineering and Building Technology (KICT), Goyang, Republic of Korea*

ARTICLE INFO

Article history:
Received 24 March 2021
Revised 11 May 2021
Accepted 22 May 2021
Available online 26 May 2021

Keywords:
Adsorption
Ce-MOF
Dyes
Magnetic composite
Mechanism

ABSTRACT

The presence of synthetic dyes in water leads to health and ecological concerns due to their toxic and carcinogenic effects. For the remediation of coloured wastewater, we have fabricated a Ce-MOF@Fe_3O_4@activated carbon composite. The composite showed a ~97–98% removal of indigo carmine and methylene blue at pH 7, whereas it was ~83–85% for activated carbon. The adsorption and kinetic data followed the Temkin and Elovich models, respectively. Which suggested the involvement of physicochemical forces in the adsorption process. The thermodynamic study confirmed the adsorption process to be endothermic, where the adsorption performance improved with the increasing temperature. The increased intensity of the band at 824 cm^{-1} (C—H) and 1004 cm^{-1} (aromatic C═C) in the Raman spectra confirmed the adsorption of dyes onto the adsorbent. Dye adsorption was further confirmed by the N 1s peak at 400 eV for C—N═C in the dye-adsorbed composite. The shift in the binding energy of Fe 2p and Ce 3d peaks by 0.3–0.4 eV concluded the involvement of electrostatic and cation-π interactions in the adsorption process. A ~90–98% dye removal capacity of the adsorbent even in the fourth cycle made it a highly stable and reusable adsorbent for remediation of coloured wastewater.

1. Introduction

Water pollution is a global challenge [1]. Coloured wastewater produced in cosmetic, textile, and paint industries harms socio-environmental sustainability and human health [2]. Organic dyes have toxic and carcinogenic effects, which cause permanent health damage after prolonged exposure [3]. Dye pollution causes severe loss of water transparency and dissolved oxygen, which have detrimental effects on aquatic flora and fauna. The decreased photosynthetic activity due to poor sunlight penetration through water leads to oxygen deficiency and alters the biological cycles of aquatic biota [4,5]. Different treatment technologies like photocatalysis [6], adsorption [7], precipitation [8], electrochemical techniques [9], and membrane filtration [10] have been explored for the removal of organic pollutants from wastewater. Among these, adsorption is the most preferred technique due to its simplicity, affordability, and efficiency for dye removal [2].

Metal-organic frameworks (MOFs) are crystalline microporous coordination polymers composed of metal ions/clusters (nodes) and organic ligands (linkers). MOFs for wastewater treatment have gained momentum due to their high adsorption capacity, relatively high water stability, and fine-tuning for specific host–guest interactions [11]. Cerium-based MOFs are known to have a high adsorption capacity for organic dyes [2]. To further improvement in the adsorption performance, carbon-rich adsorbents such as activated carbon (AC) are used to modify MOF-based adsorbents. AC/metal oxide composites are reported as efficient adsorbents for organic dye removal [12–14]. Altintig et al. reported excellent adsorption performance for malachite green over Fe_3O_4-AC [12]. Similarly, Tuzen et al. reported an adsorption capacity of 324.6 mg g^{-1} for rhodamine B with a magnetic AC-CeO_2 nanocomposite [14]. Magnetic composites are highly recommended for an easy recovery of dye-loaded adsorbent using an external magnetic field [15], whereas AC provides additional binding sites for the adsorptive removal of organic dyes. These studies provide a great deal of information on the adsorption capacity, parameters optimizations, and probable mechanisms. But, many of these studies lack detailed investigation on the adsorption mechanism and the reusability of the materials. The effect of regeneration on the material structure and functionalities are also not explored in these published works.

In this work, a new magnetic Ce-MOF@Fe_3O_4@AC composite was synthesized for the adsorptive removal of organic dyes. The composite was characterized by multiple analytical techniques to

---

* Corresponding author.
E-mail addresses: viltresh@mcmaster.ca (H. Viltres), zleyva@ipn.mx (C. Leyva).

https://doi.org/10.1016/j.molliq.2021.116578
0167-7322/

evaluate its structural and functional characteristics. The adsorptive performance was evaluated using two organic dyes, i.e., a cationic dye (methylene blue) and an anionic dye (indigo carmine). The adsorption kinetics, isotherms, thermodynamics, and reusability of the Ce-MOF@Fe_3O_4@AC were also studied. Moreover, the adsorption process was tested using spectroscopic techniques. The reusability of the adsorbent was evaluated over multiple cycles. The study confirmed that the synthesized composite is highly stable and suitable for the treatment of dye-rich wastewater.

2. Materials and method

2.1. Chemicals and reagents

Indigo carmine (IC) and methylene blue (MB) were supplied by MERCK, USA. Iron chloride hexahydrate ($FeCl_3{\cdot}6H_2O$, purity ≥ 99%), iron sulphate heptahydrate ($FeSO_4{\cdot}7H_2O$, purity ≥ 99.0%), sodium hydroxide pellets (NaOH, purity ≥ 97.0%), Activated Carbon (AC), trimesic acid (H_3BTC, purity 95%), and anhydrous dimethylformamide (DMF, purity 99.8%) were supplied by Sigma-Aldrich, Germany. Methanol and ethanol were purchased from Baker® and Mayer®, respectively. The reagents were used without further purification.

2.2. Synthesis of adsorbents

Magnetite nanoparticles (Fe_3O_4): Fe_3O_4 nanoparticles were synthesized by the co-precipitation method. A 4.53 g of $FeCl_3{\cdot}6H_2O$ was dissolved into 100 mL of acidified water under N_2 bubbling for 0.25 h. Then, a solution of $FeSO_4{\cdot}7H_2O$ (2.78 g in 100 mL of distilled water) was added. To it, 300 mL of NaOH solution (1.25 mol L^{-1}) was added under N_2 bubbling. The entire process was carried out with constant stirring and constant flow of N_2 for an inert atmosphere. After 1 h, the black precipitate was separated magnetically, washed with water until pH 7, and dried under vacuum for 24 h at 50 °C [16].

Magnetite-activated carbon composite (Fe_3O_4@AC): The previous procedure (co-precipitation) was employed for the synthesis of Fe_3O_4@AC, but modified by adding 0.5 g of activated carbon in $FeSO_4{\cdot}7H_2O$ solution. After 1 h of N_2 bubbling, the mixture was aged for 24 h in the dark at room temperature. The solid obtained was separated magnetically, washed 6 times with water and 3 times with ethanol, and dried at 50 °C for 24 h.

Ce-MOF: Exactly 2.6 g of $Ce(NO_3)_3{\cdot}6H_2O$ and 1.68 g of H_3BTC were dissolved in 40 mL of DMF under sonication. The solution was heated in an oven at 120 °C for 24 h. The supernatant solid was washed with DMF (three times) and methanol (three times), followed by drying at 50 °C for 24 h.

Ce-MOF@Fe_3O_4@AC: For the nanocomposite formation, 1.0 g of Ce-MOF and 0.5 g of Fe_3O_4@AC were uniformly dispersed in 50 mL of deionized water by sonication, which was followed by stirring for 3 h. The product was separated magnetically, washed three times with water, and dried at 50 °C for 24 h. Scheme 1 shows a representation of the synthesis of Ce-MOF@Fe_3O_4@AC.

2.3. Analytical instruments

Detailed information on analytical instruments is available in **Section S1**.

2.4. Experimental procedure

Detailed information on the experimental procedure is available in **Section S2**. In general, a known mass of the adsorbent was added to a dye solution with a specific pH value and stirred for 3 h. After 3 h of stirring, the adsorbent was separated with an external magnet, and the aqueous phase was analyzed by spectrophotometry. The spectra were recorded in a range of 200–800 nm, and the dye concentration was determined by monitoring the absorbance at $\lambda = 615$ and 664 nm for IC and MB, respectively. Duplicate readings were taken for each sample. The reusability of the synthesized Ce-MOF@Fe_3O_4@AC composite was studied for four adsorption–desorption cycles. The dye-loaded Ce-MOF@Fe_3O_4@AC composite was washed with methanol (99%) for 1 h, dried at room temperature, and tested for the next cycle.

3. Results and discussion

3.1. Characterization of adsorbents

The Fourier-transform infrared (FTIR) spectra of adsorbents are shown in Fig. 1**A** and assignments are available in **Table S2**. For AC, bands in the range of 3200–3650 cm^{-1} were assigned to the O—H stretching of phenols and water molecules. The C—H asymmetric stretching vibration was associated with the band at 2908 cm^{-1}. The bands at 1635 and 1552 cm^{-1} were related to the bending mode of H_2O and stretching mode of aromatic —C=C, respectively. The band at 1150 cm^{-1} can also be associated with the ether C—O stretching vibrations (—C—O—C— ring) [17,18]. For Fe_3O_4 nanoparticles, an intense band at 544 cm^{-1} was observed for Fe–O stretching vibrations [19]. The characteristic bands of Fe_3O_4 and AC

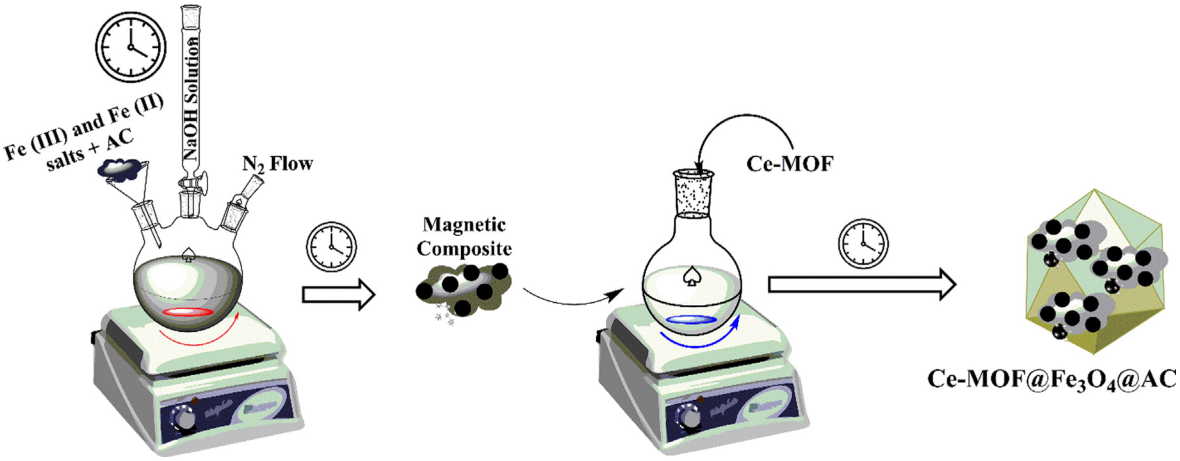

Scheme 1. Schematic representation of the synthesis of Ce-MOF@Fe_3O_4@AC.

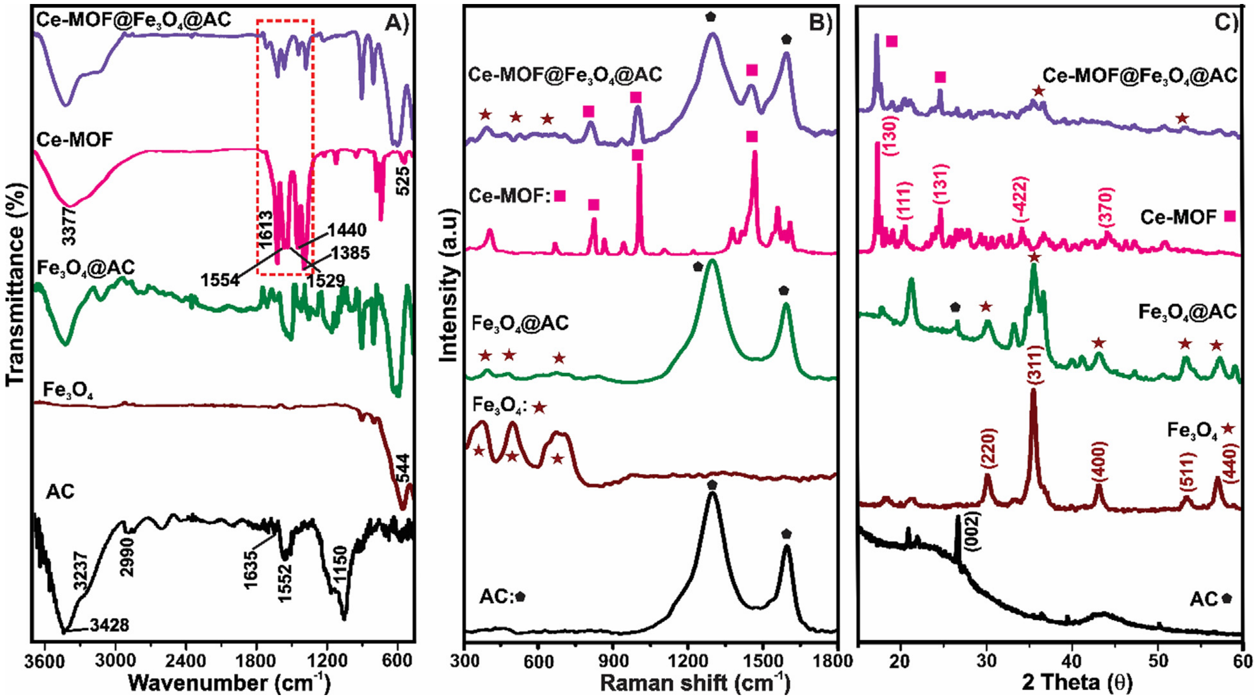

Fig. 1. (**A**) FTIR, (**B**) Raman spectra, and (**C**) XRD patterns of adsorbents.

remained intact in the Fe_3O_4@AC. The Ce-MOF spectrum has a broad band at 3377 cm^{-1} for O—H stretching of the coordinated water molecules. Characteristics peaks related to the carboxylate groups appeared at 1613 cm^{-1} (asymmetric) and 1440 and 1385 cm^{-1} (symmetric). The absence of a band at 1714 cm^{-1} ($\upsilon_{C=O}$, the vibration of carboxylic groups in the free H_3BTC ligand) indicated the formation of Ce–carboxylate bonds in the MOF. The bands at 1554 and 1529 cm^{-1} were attributed to the C=C stretching vibrations from the aromatic ring of ligands [20,21]. The peak at 530 cm^{-1} was assigned to the stretching vibration of Ce—O [22]. The characteristic bands of Fe_3O_4@AC and Ce-MOF were observed in the Ce-MOF@Fe_3O_4@AC composite.

Raman spectra are shown in Fig. 1**B**. All samples with AC exhibited two characteristic bands at 1295 and 1590 cm^{-1}, denoted as the D-band and G-band, respectively. The G-band (vibrational modes having E_{2g} symmetry) originating from the stretching vibration of all sp^2-bonded pairs. The D-band (lattice breathing mode having A_{1g} symmetry) was associated with the sp^3 defect sites, indicating the presence of disorder [23]. For Fe_3O_4, three bands at 368, 495, and 674 cm^{-1} were observed. The bands at 368 and 495 cm^{-1} were attributed to the E_g and $T_{2g}(2)$ modes for the symmetric and asymmetric bending of oxygen with respect to iron in the tetrahedral void, respectively. The band at 674 cm^{-1} was assigned to the A_{1g} mode for the symmetric stretching of the oxygen atoms in the tetrahedral FeO_4 group [24]. Raman spectrum of the Ce-MOF showed a band at 824 cm^{-1} assigned to the out-of-plane C—H bending vibration. The bands at 1004 and 1617 cm^{-1} were ascribed to the C=C stretching modes of the benzene ring. The bands at 1450 and 1550 cm^{-1} were assigned to the symmetric and asymmetric modes of the carboxylate units, respectively. The band at ~430 cm^{-1} was assigned to the symmetric stretching vibrations (IF_{2g}) mode of CeO_2 lattice [25,26]. The final composite has the active modes for the Fe_3O_4@AC and Ce-MOF. The results corroborated the synthesis of the final magnetic composite, Ce-MOF@Fe_3O_4@AC.

The crystallinity and phase purity of AC, Ce-MOF, Fe_3O_4, Fe_3O_4@AC and Ce-MOF@Fe_3O_4@AC were investigated using powdered X-ray diffraction (XRD) (Fig. 1**C**). The pattern of AC revealed amorphous features with a peak at 26° for 002 Bragg reflection [27]. In the XRD pattern of Fe_3O_4, the diffraction peaks at $2\theta = 30.12°$, 35.48°, 43.12°, 57.02°, and 62.62° were assigned to the 220, 311, 400, 511, and 440 reflections of Fe_3O_4 (JCPDS #88-0866), respectively [28]. The Fe_3O_4@AC composite retained the amorphous feature of AC and the crystalline Bragg reflections of Fe_3O_4. The diffraction peaks of synthesized Ce-MOF matched well with the simulated pattern for Ce(1,3,5-BTC)$(H_2O)_6$ (**Fig. S2**). The principal peaks at 11.2° and 17.4° confirmed good MOF crystallinity. The diffraction peaks of Ce-MOF@Fe_3O_4@AC showed the characteristic diffraction peaks of Ce-MOF and Fe_3O_4@AC.

The thermal stability of Fe_3O_4@AC, Ce-MOF, and Ce-MOF@Fe_3O_4@AC was evaluated by thermogravimetric analysis (TGA) (Fig. 2**A**). The Fe_3O_4, AC, and Fe_3O_4@AC were characterized by three weight loss regions in the temperature range of 30–200, 200–400, and 400–600 °C (**Fig. S1A, Table S3**). The first region in Fe_3O_4@AC was due to the evaporation of water molecules. The second region was assigned to the destruction of the labile oxygen-containing functional groups. The third region was due to the complete AC oxidation at 550 °C [29,30]. For Ce-MOF, the structure obtained was consistent with the literature. The loss of adsorbed water and DMF was observed over a temperature range of 150–250 °C. Beyond 370 °C, the MOF structure collapsed due to the decomposition of the framework [20]. The Ce-MOF@Fe_3O_4@AC composite showed an initial ~13% weight loss due to the removal of water molecules around 100 °C. The decomposition of the final composite started at 470 °C as opposed to 370 °C for Ce-MOF, which demonstrated an improvement in the thermal stability of the final composite.

The magnetic properties of materials were measured at 5 K (**Fig. S1B**) and 300 K (Fig. 2**B**). The hysteresis curves showed a superparamagnetic behaviour for all samples with a sigmoidal form, where the remanence and coercivity were close to zero at room temperature. **Tables S4 and S5** showed values of the saturation magnetization (μ_s), coercivity (H_c), and remanence magnetization (μ_r). The saturation magnetization of Fe_3O_4 (69.30 emu g^{-1})

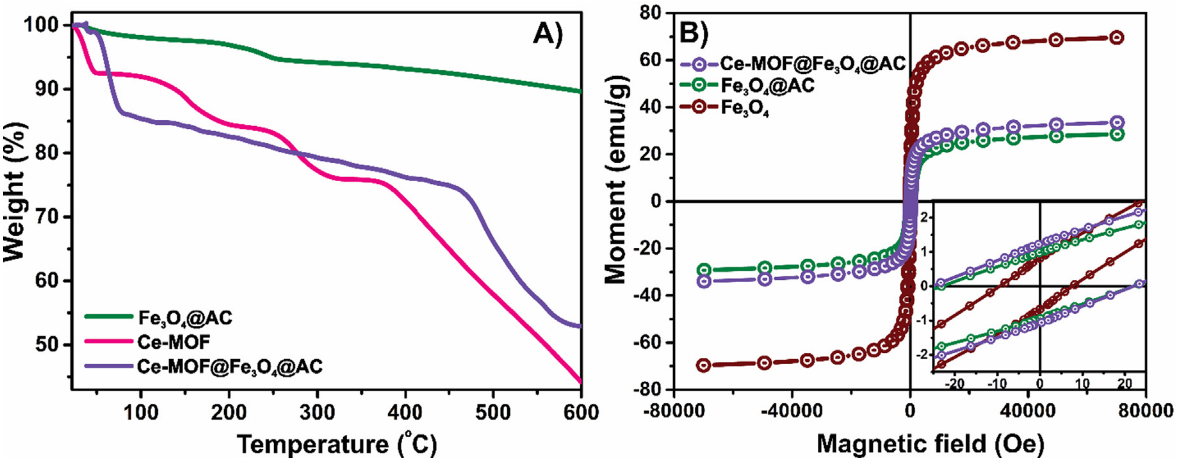

Fig. 2. (**A**) TGA and (**B**) VSM of adsorbents.

was found to be lower than the bulk Fe_3O_4 (80.0 emu g^{-1}) [31]. The saturation magnetization of Fe_3O_4@AC (28.77 emu g^{-1}) and Ce-MOF@Fe_3O_4@AC (21.39 emu g^{-1}) was even lower than the Fe_3O_4. Thus, the magnetic property of Fe_3O_4@AC and Ce-MOF@Fe_3O_4@AC decreased due to the incorporation of non-magnetic mass in composites. The superparamagnetic properties of Ce-MOF@Fe_3O_4@AC made it a potential adsorbent for aqueous systems with excellent recovery.

The surface elemental composition and the oxidation states of constituent elements were studied by X-ray photoelectron spectroscopy (XPS). The XPS survey profiles confirmed C, O, Fe, and Ce in different samples (Fig. 3**A** and **Table S6**). The high-resolution C 1s spectrum of Ce-MOF@Fe_3O_4@AC was deconvoluted into four contributions at 284.8, 286.1, 289.0, and 291.2 eV (Fig. 3**B**). The first peak was assigned to the aromatic C═C/C—C of trimesate linkers and graphitic carbon in AC [32]. The peaks at 286.1 and 289.0 eV were assigned to C—O and C═O, respectively. The low-intensity peak at 291.2 eV was ascribed to the π-π^* bonding moieties [33]. The O 1s spectrum has four peaks at 530.3, 531.5, 532.3, and 533.4 eV for Ce—O/Fe—O, C═O, C—OH, and adsorbed H_2O molecules, respectively (Fig. 3**C**) [32,34]. The high-resolution Fe $2p_{2/3}$ spectrum from the high-spin Fe^{3+} compound was fitted using the Gupta and Sen multiplets [33,35]. The resulting fit for $Fe2p_{3/2}$ in Ce-MOF@Fe_3O_4@AC suggested the presence of Fe_3O_4 and oxy-hydroxide components (Fig. 3**D**, **Table S7**). The Fe^{3+}/Fe^{2+} ratio of 2.1:1 was close to the expected ratio of 2:1 in the Fe_3O_4 phase [35]. The high-resolution Ce $3d_{5/2}$ spectrum was deconvoluted into four peaks (Fig. 3**E**). The results suggested that Ce was present as Ce^{3+} and Ce^{4+} ions. The peaks at 883.2 and 885.6 eV were assigned to the Ce^{3+}, whereas the peaks at 881.7 and 887.5 eV were ascribed to the Ce^{4+} sites [32,36,37]. Therefore, Ce-MOF@Fe_3O_4@AC has Ce^{3+} and Ce^{4+} oxidation states as metal centres.

3.2. Stability of Ce-MOF

The stability of the Ce-MOF at different pH values was evaluated by FTIR and XRD (Fig. 4). Fig. 4**A** shows the FTIR spectra of Ce-MOF before and after soaking in the pH range of 2–14. In the pH range of 2–12, similar Ce-MOF spectra were observed with slight variation in the 3450 cm^{-1} band due to variable water content. At pH 14, the bands corresponding to the asymmetric and symmetric stretching of the Ce—carboxylate bonds disappeared. Moreover, the peak at 525 cm^{-1} for Ce—O increased due to the formation of CeO_2. The MOF structure remained intact in the pH range of 1–12, implying high chemical stability of Ce-MOF (Fig. 4**B**). The MOF structure deteriorated at pH 14 with the appearance of new diffraction peaks at 28.2°, 32.9°, and 47.4° for the reflections, 111, 200, and 220 from the cubic phase of CeO_2, respectively (JCPDS #34-0394). Ce-MOF was transformed to CeO_2 at pH 14 with the destruction of the MOF structure [38,39] therefore, Ce-MOF was stable in the pH range of 2–12.

3.3. Effect of parameters

The effect of adsorbent dosage was studied by varying the adsorbent mass in the range of 3–50 mg (Fig. 5**A**). The dye removal efficiency improved with the increasing adsorbent mass until 20 mg due to the addition of new adsorption sites. After 20 mg dosage, the removal performance saturated due to the unavailability of dye molecules for adsorption. The optimal adsorbent dosage was 20 mg for both dyes, where ~100% removal was achieved. The effect of initial dye concentration was tested in the range of 10–90 mg L^{-1} (Fig. 5**B**). The removal efficiency of >99% for a 10 mg L^{-1} dye solution decreased slightly with the increasing concentration. It was due to the saturation of all adsorption sites at a higher concentration and the unavailability of adsorption sites for the remaining dye molecules in the aqueous phase. Nevertheless, the removal efficiency was above 90% in the entire concentration range for MB and IC.

Ce-MOF@Fe_3O_4@AC was tested in a wide pH range of 2–10 (Fig. 5**C**). The adsorbent showed removal efficiency > 80% for both IC and MB in the entire pH range. The pH variation did not affect the IC removal process, whereas the MB adsorption efficiency improved at a higher pH. The isoelectric point of the composite was pH 5 therefore, the surface was positively charged below pH 5 and negatively charged above it [40]. In the pH range of 2–4, the positively charged adsorbent surface repulsed MB molecules (cationic dye), leading to a low removal efficiency. Above pH 5, the negatively charged composite interacted with the MB dye through electrostatic forces, which enhanced the adsorption performance (~100% MB removal). Meanwhile, IC is an anionic dye, which is favourably adsorbed on the positively charged adsorbent surface via electrostatic interaction below pH 5. However, at pH > 5, an insignificant drop in the adsorption performance suggested the involvement of other binding forces like cation-π and π-π interactions. The removal performance of AC and Fe_3O_4@AC was compared with the Ce-MOF@Fe_3O_4@AC (**Fig. S3**). The study revealed that the MOF@Fe_3O_4@AC exhibited the highest dye removal efficiency therefore, the magnetic composite, MOF@Fe_3O_4@AC, was a superior adsorbent for IC and MB dyes in a wide pH range. The effect of contact time on the adsorption performance

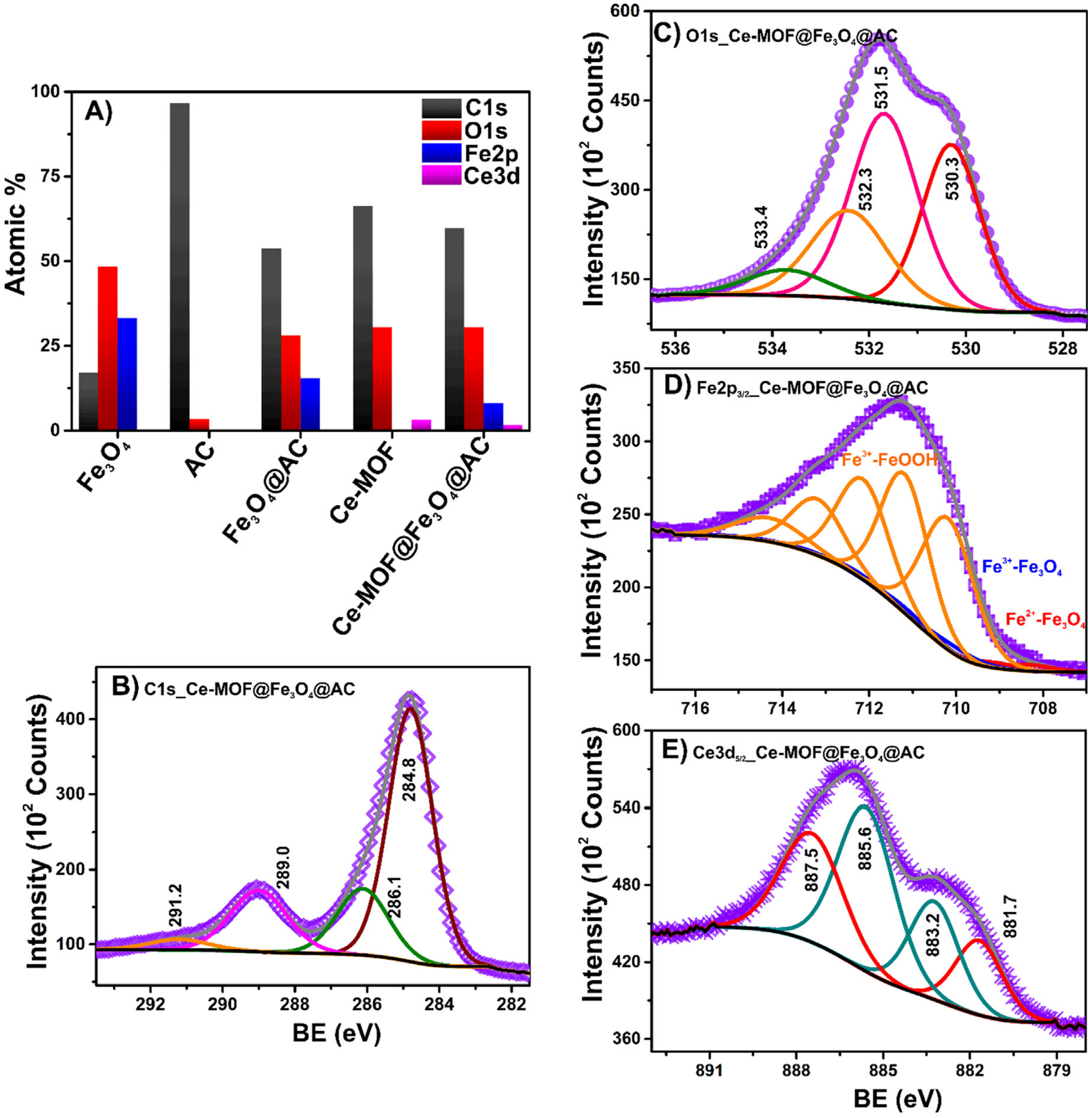

Fig. 3. (**A**) Element quantification from survey spectra of AC, Fe_3O_4, Fe_3O_4@AC, Ce-MOF, and Ce-MOF@Fe_3O_4@AC, high-resolution spectra of Ce-MOF@Fe_3O_4@AC in the (**B**) C 1s, (**C**) O 1s, (**D**) Fe 2p, and (**E**) Ce 3d regions.

is shown in Fig. 5**D**. The dye removal efficiency increased with the increasing agitation time as the adsorbate-adsorbent interactions improved with time. A ∼100% removal was observed after 3.5 h of agitation for both dyes. These results concluded that 20 mg of adsorbent, 3 h of agitation time, and a pH range of 5–7 are the optimal conditions for the maximum dye removal efficiency.

3.4. Adsorption kinetics

The pseudo-first-order (PFOM), pseudo-second-order (PSOM), Elovich, and Intra-particle diffusion (IPD) [41] models were employed to study the adsorption kinetics (Fig. 6). The equations and derived parameters for these models are listed in **Table S8**. Based on the correlation coefficient (R^2), the kinetic data for IC and MB fit the PFO ($R^2 \sim 0.98$) and the Elovich model ($R^2 \sim 0.95$), respectively (**Table S9**). Moreover, the q_e value from the PFO model was in close agreement with the experimental q_e value for IC. For MB, the q_e value from the Elovich model agreed with the experimental value. Since the synthesized composite is a porous material, diffusion could influence the adsorption process. For this reason, the kinetic data were fitted to the IPD model to study the role of diffusion in the dye adsorption process. The data were fitted in three regions, which were regarded as three adsorption processes for IC and MB (Fig. 5**G and 5H**)). The rate constant (K_{ip}) was in the order of $K_{ip2} > K_{ip1} > K_{ip3}$ for both IC and MB dyes (**Table S9**). In the first step (K_{ip1}), dye molecules rapidly migrated from the bulk aqueous phase to the composite surface until the surface saturated. In the second step (K_{ip2}), dye molecules entered the pores of the composite with increasing resistance to diffusion. In the last step (K_{ip3}), dye molecules diffused into the pores until the equilibrium was achieved [42]. The dye molecules interacted with the binding sites on the surface and in the pores via physicochemical forces like electrostatic, cation-π, and π-π interactions.

3.5. Adsorption isotherm

The nature of the adsorption process was predicted by fitting the experimental data to the Langmuir, Freundlich, Temkin, and

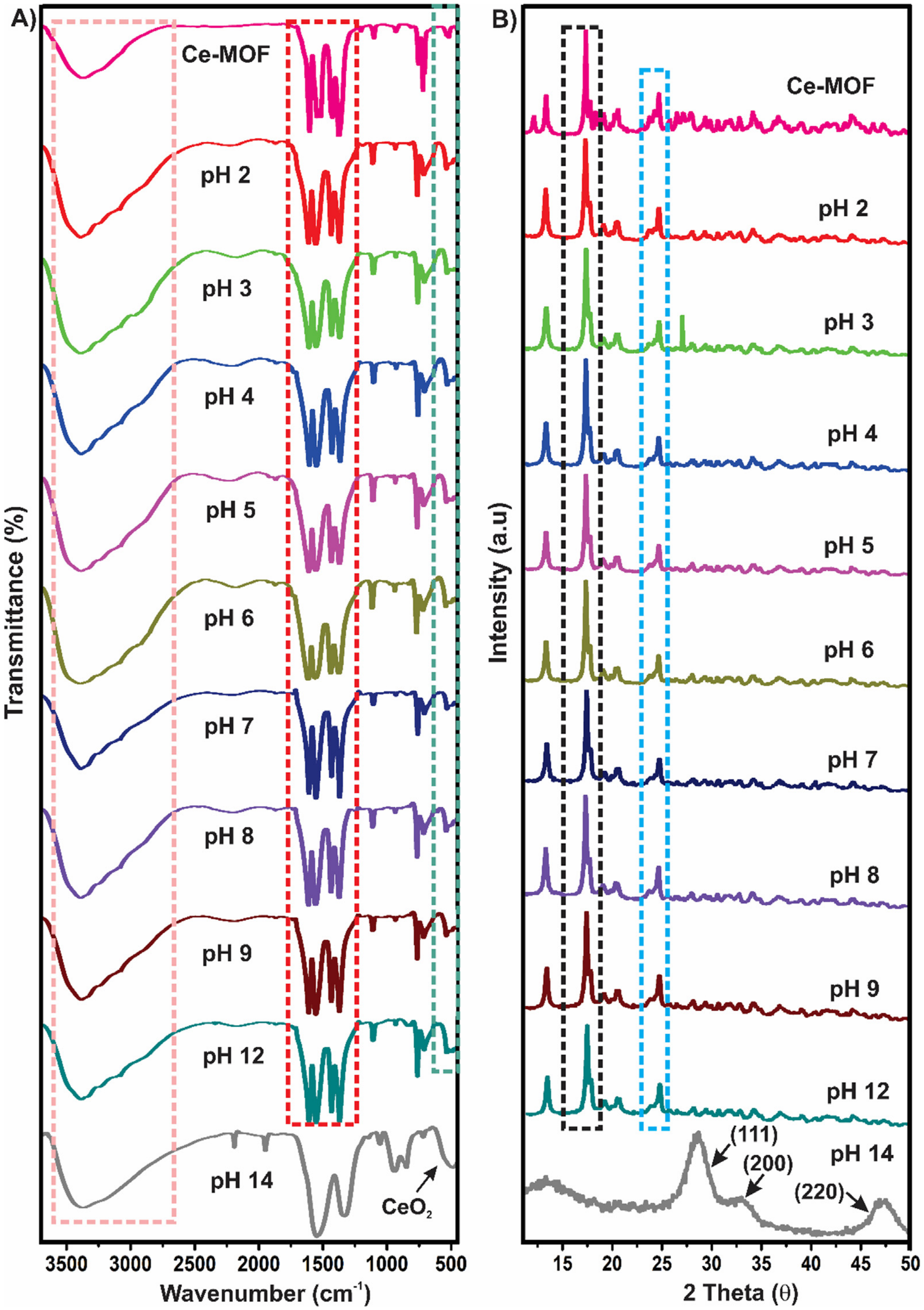

Fig. 4. (**A**) FTIR spectra and (**B**) XRD patterns of Ce-MOF soaked in aqueous solutions of different pH values for 12 h.

Dubinin–Radushkevich models (Fig. 7, **Table S10**) [43]. The Langmuir model applies to adsorbents with monolayer adsorbate coverage over homogenous adsorption sites. For both IC and MB, the Langmuir model provided a good fit. The maximum adsorption capacity was 85.5 and 84.9 mg g^{-1} for IC and MB, respectively (**Table S11**). The separation factor (R_L) remained between 0 and 1, suggesting a favourable adsorption process for IC and MB. The adsorption intensity or Langmuir coefficient (K_L) indicates the strength of adsorbate-adsorbent interaction. For both dyes, the calculated K_L was relatively small due to the involvement of weak physicochemical forces. Also, the free Gibbs energy values were negative, suggesting that the adsorption process was spontaneous. The Freundlich model is suitable for adsorbents with multilayer adsorbate coverage over heterogeneous adsorption sites. Due to the heterogeneity of the composite, experimental data also fit the Freundlich model. Therefore, the adsorption process was governed by physicochemical forces. The Temkin model considers the effects of indirect adsorbate/adsorbate interactions during the adsorption process. The heat of adsorption (B) provides information about the adsorption process. For $B < 1$ kcal mol^{-1}, the adsorption occurs mainly by physical interactions, whereas for $B > 20$ kcal mol^{-1}, the process is governed by chemical forces. For both IC and MB,

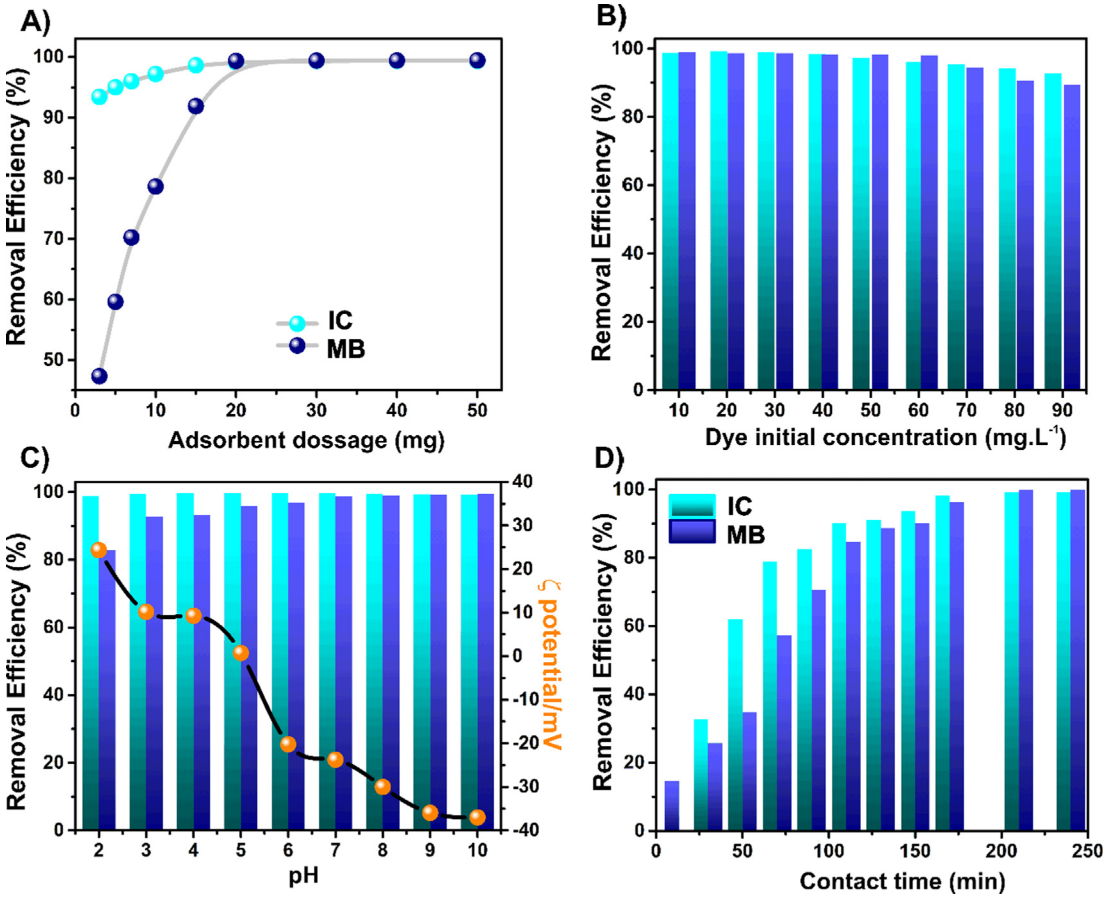

Fig. 5. Effect of (**A**) Adsorbent dosage; (**B**) Dye concentration; (**C**) pH; (**D**) Contact time on Indigo carmine (IC) and Methylene blue (MB) removal efficiency over Ce-MOF@Fe_3O_4@AC. Conditions (unless specified): Time = 3 h, pH 7, T = 298 K, C_0: 50 mg L^{-1} of dye, 20 mg of adsorbent.

the heat of adsorption was less than 1, which suggested physical interactions of dye molecules with the adsorbent surface. Based on the closeness of the correlation coefficient (R^2) with 1, the Temkin isotherm model was suitable for describing the adsorption process of IC (R^2 = 0.98) and MB (R^2 = 0.96) dye. It indicated the involvement of physical forces in the adsorption of IC and MB molecules over Ce-MOF@Fe_3O_4@AC.

3.6. Effect of temperature

The effect of temperature on the adsorption of IC and MB was studied in the range of 300–343 K. Removal efficiency of IC and MB increased slightly with the increasing temperature (Fig. 8**A and 8B**) due to the endothermic nature of the adsorption process. Thermodynamics parameters are important for understanding the nature of the adsorption mechanism. The Vańt Hoff equation (**Eq. (1)**) was used to evaluate the thermodynamic parameters for IC and MB dye (Fig. 8**C and D**). The change in free energy ($\Delta G°$), change in enthalpy ($\Delta H°$), and change in entropy ($\Delta S°$) were calculated employing Eqs. (1) and (2) [43].

$$ln(K_c) = \frac{\Delta S^{\circ}}{R} - \frac{\Delta H^{\circ}}{RT} \quad (1)$$

$$\Delta G^{\circ} = \Delta H^{\circ} - T\Delta S^{\circ} \quad (2)$$

where K_c ($K_c = Q_e/C_e$) is the equilibrium constant, R (8.314 J mol^{-1} K^{-1}) is the gas constant, and T (K) is the adsorption temperature. The thermodynamic parameters and the correlation coefficient value are listed in **Table S12**. The values of $\Delta H°$ and $\Delta S°$ were determined from the slope ($\Delta H/R$) and the intercept ($\Delta S/R$) of the plot between $\ln(Q_e/C_e)$ and $1/T$, respectively. The positive $\Delta H°$ value indicated the endothermic nature of the adsorption process. On the other hand, the positive value of $\Delta S°$ suggested an increase in randomness at the solid-solution interface during the adsorption process [44]. The negative value of $\Delta G°$ indicated the spontaneous nature of the adsorption process. The increase in the absolute value of free energy with temperature suggested that the adsorption is improved at a higher temperature, resulting in higher removal efficiency [45]. These results may be related to the increase in the diffusion potential of the dye molecules at a higher temperature, facilitating dye molecules near the adsorption sites.

3.7. Adsorption mechanism

The dye adsorption mechanism over Ce-MOF@Fe_3O_4@AC was studied using Raman and XPS spectroscopy (Fig. 9). Raman spectra of adsorbent before and after dye adsorption are illustrated in Fig. 9**C**. The band at 824 cm^{-1} for C—H increased after IC and MB adsorption. The intensity of 1004 cm^{-1} for C=C improved due to the presence of benzene rings in the adsorbed IC and MB molecules. The N atoms of IC and MB dyes (Fig. 9**A and B**) were studied through HRXPS N 1s analysis (Fig. 9**D**). Since there was an absence of N in the adsorbent, the dye adsorption was confirmed by the N 1s peak at 400 eV for the C—N=C in MB and IC dyes [46]. The two peaks in the Ce 3d HRXPS spectrum of the new magnetic composite at 886.3 and 904.6 eV were assigned to the Ce $3d_{5/2}$ and Ce $3d_{3/2}$, respectively (Fig. 9**E**). After the adsorption of MB and IC dyes, the binding energy of the peaks reached 885.9 and 904.3 eV, respec-

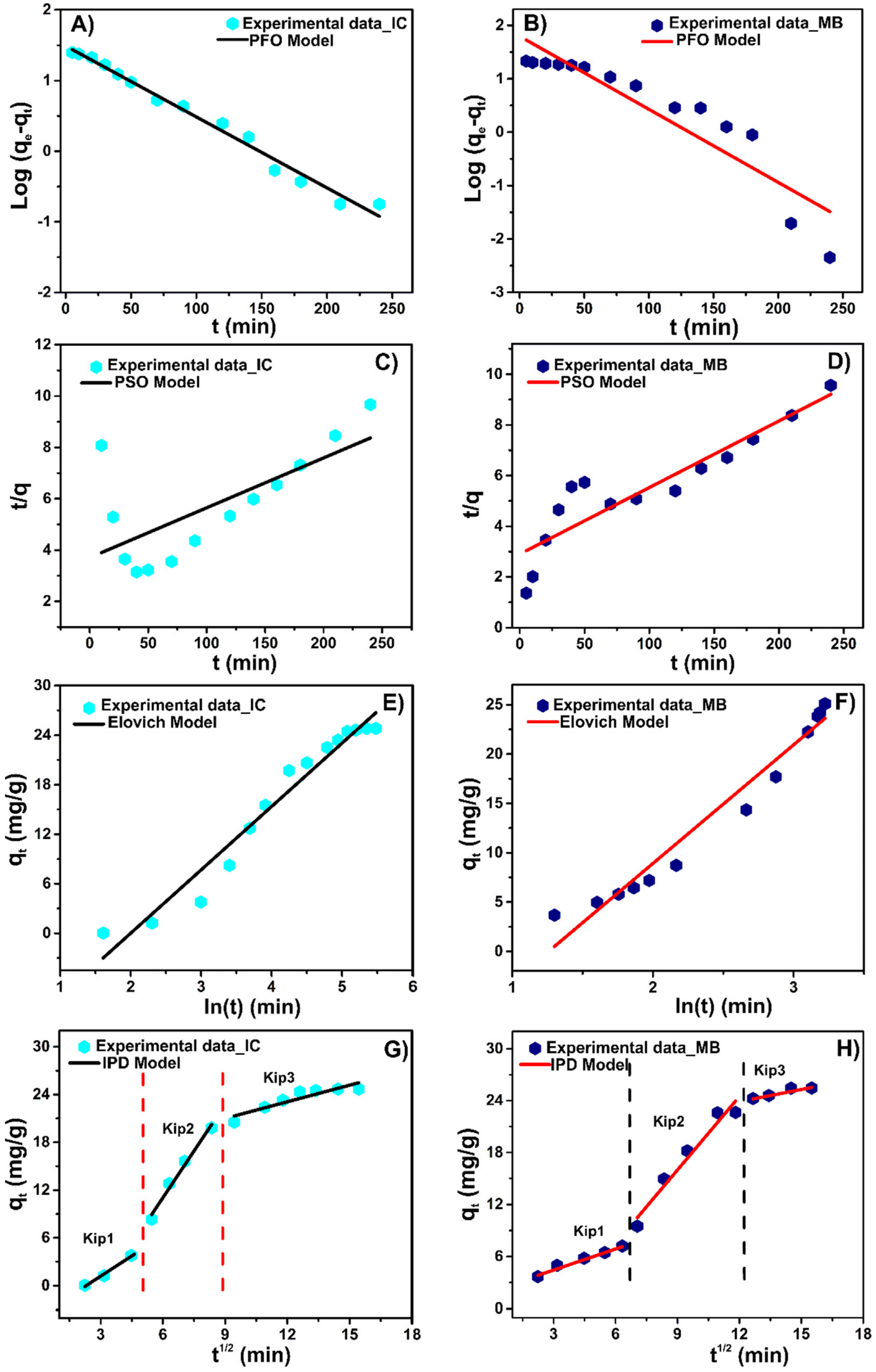

Fig. 6. Kinetic models for Indigo carmine (IC) and Methylene blue (MB) adsorption onto Ce-MOF@Fe_3O_4@AC. Conditions: pH 7, T = 298 K, C_0: 50 mg L^{-1} of dye, 20 mg of adsorbent.

tively. The shift in the binding energy of Ce 3d peaks by 0.3–0.4 eV was due to the increase in the electron density around the Ce ions. This increase in the electron density was due to cation-π interactions between Ce-sites and π-electrons in the benzene ring of organic dyes [47]. The HRXPS Fe 2p spectrum of composite showed peaks at 711.2 and 724.9 eV for Fe $2p_{3/2}$ and Fe $2p_{1/2}$, respectively. The binding energy of Fe 2p peaks also shifted by 0.3–0.4 eV after dye adsorption, due to the contribution of electron density from

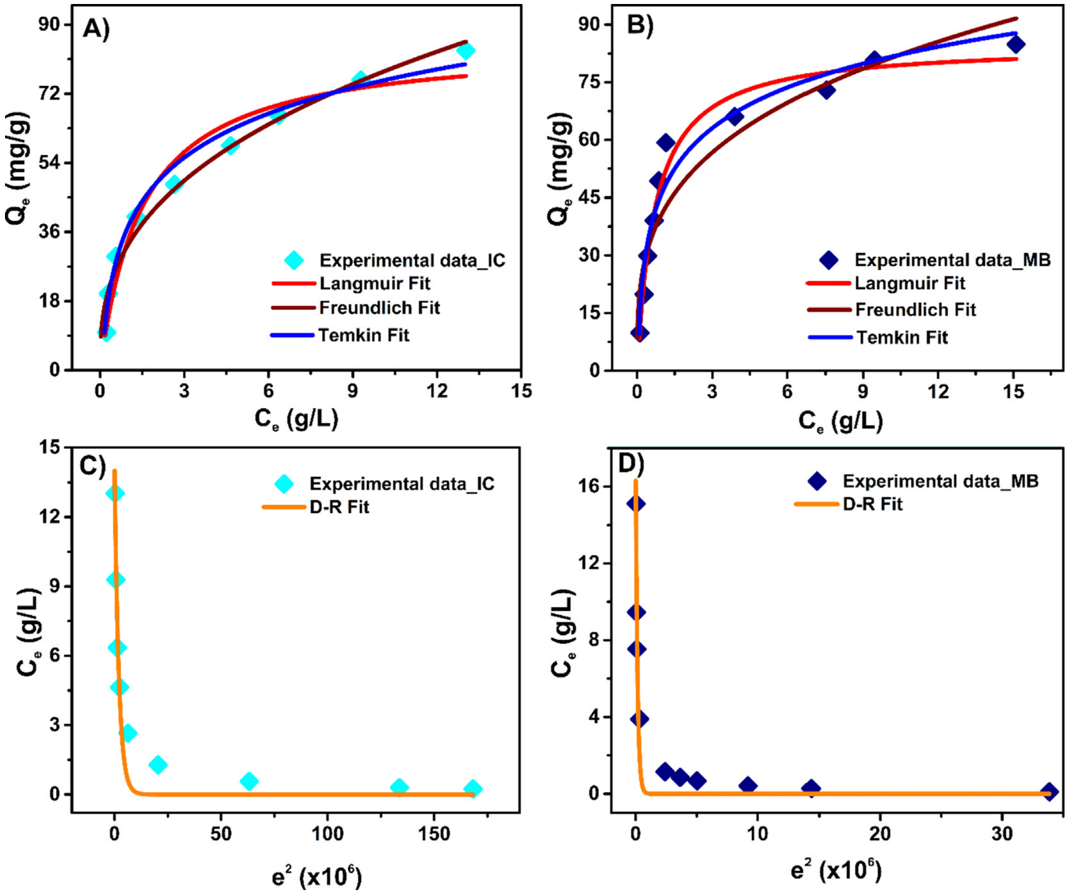

Fig. 7. Langmuir, Freundlich, and Temkin fits for (**A**) Indigo carmine (IC); (**B**) Methylene blue, and Dubinin-Radushkevich fit for (**C**) Indigo carmine (IC); (**D**) Methylene blue. Conditions: Time = 3 h, pH 7, *T* = 298 K, 20 mg of adsorbent.

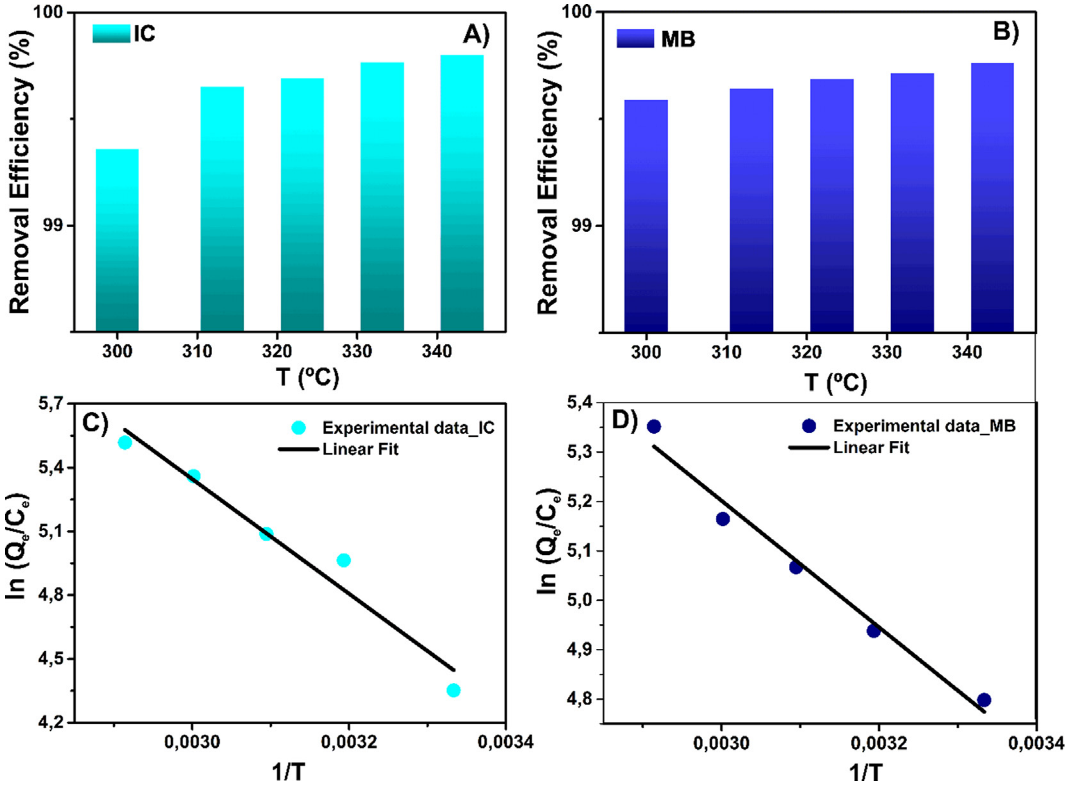

Fig. 8. Effect of temperature on (**A**) Indigo carmine (IC); (**B**) Methylene blue adsorption, and the standard free energy change of adsorption for (**C**) Indigo carmine (IC); (**D**) Methylene blue adsorption. Conditions: Time = 3 h, pH 7, C_0: 50 mg L^{-1} of dye, 20 mg of adsorbent.

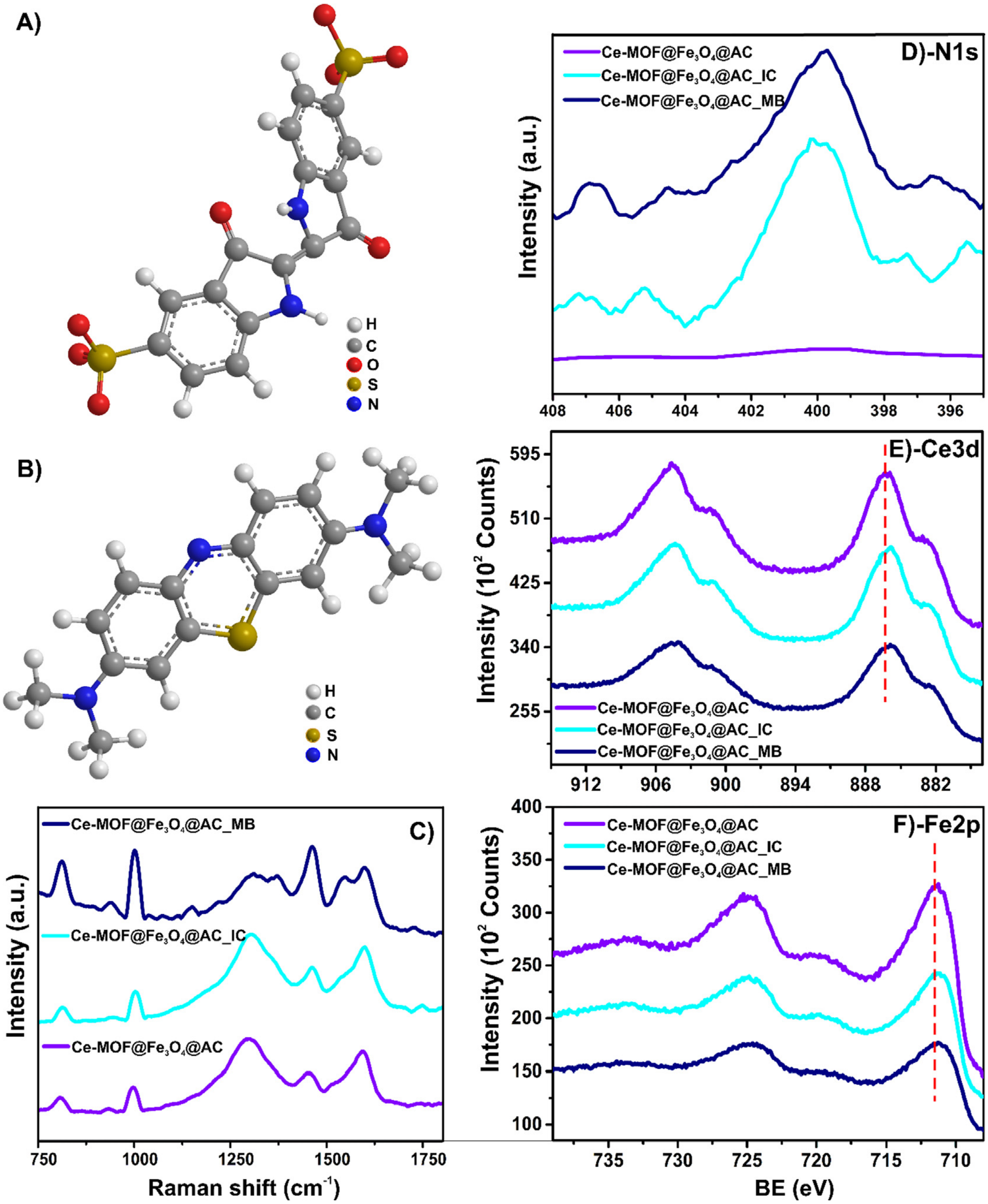

Fig. 9. Molecular structure of (**A**) Indigo carmine (IC); (**B**) Methylene blue; (**C**) Raman spectra; (**D**) N 1s; (**E**) Ce 3d; (**F**) Fe 2p high-resolution signals for Ce-MOF@Fe$_3$O$_4$@AC before and after dye adsorption.

dye molecules to Fe ions in the Fe$_3$O$_4$ (Fig. 9**F**). It was therefore concluded that cation-π interaction was one of the main mechanisms, apart from π-π and electrostatic interactions between charged dyes and metal sites.

3.8. Regeneration and reusability

The regeneration of the adsorbent is critical for further large-scale applications to reduce the overall cost of the water treatment procedure. The reusability of Ce-MOF@Fe$_3$O$_4$@AC was investigated for four adsorption-regeneration cycles using methanol as the desorbing agent (Fig. 10). The removal efficiency of IC and MB using Ce-MOF@Fe$_3$O$_4$@AC was 99.5% for both dyes in the first cycle. The desorption with methanol was poor in the first cycle, probably due to insufficient contact time. In the fourth cycle, the adsorption performance decreased slightly and reached 96.0 and 86.8% of IC and MB, respectively. Interestingly, the desorption efficiency started improving with each cycle. Although desorption was only partially successful, the composite showed remarkable adsorption capacity for both dyes even after four cycles. This demonstrates its potential for the removal of organic dyes over multiple cycles.

The material stability after the regeneration process was assessed by FTIR and XRD (Fig. 11). As observed in FTIR spectra (Fig. 11**A**), the final magnetic composite (Ce-MOF@Fe$_3$O$_4$@AC) was partially stable after four cycles of MB adsorption. However, no variations were observed in the FTIR spectrum of the adsorbent for IC removal. This result was consistent with the XRD patterns (Fig. 11**B**). For IC removal, major peaks in the diffraction pattern were intact after four cycles, whereas for MB, a complete loss in the MOF crystallinity was observed. The loss in the MOF

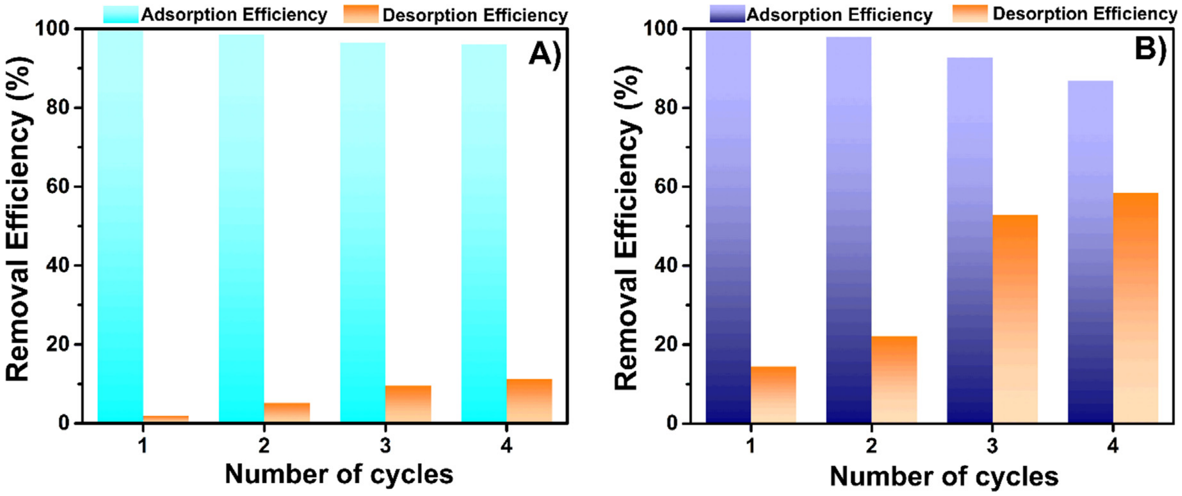

Fig. 10. Regeneration and reusability tests of Ce-MOF@Fe_3O_4@AC for removal of (**A**) Indigo carmine (IC); (**B**) Methylene blue (MB). Conditions: Time = 3 h, pH 7, T = 298 K, C_0: 50 mg L^{-1} of dye, 20 mg of adsorbent.

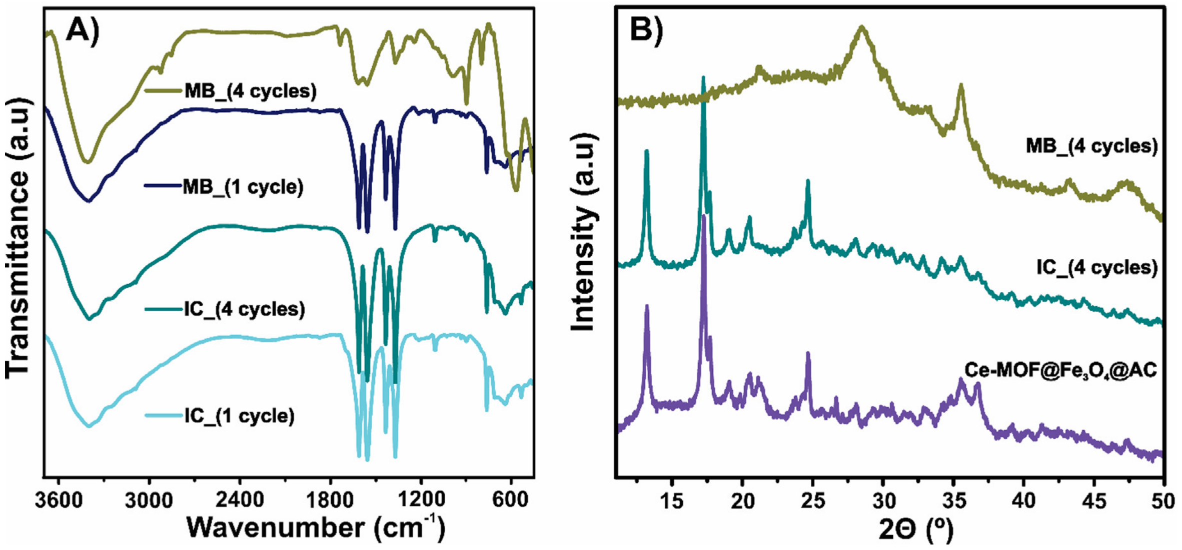

Fig. 11. (A) FTIR spectra and (B) XRD Ce-MOF@Fe_3O_4@AC after reusability tests in the removal of Indigo carmine (IC) and Methylene blue (MB).

crystallinity was probably due to the interference of cationic MB dye in the coordinative interaction between Ce nodes and trimesate linkers. Overall, the MOF@Fe_3O_4@AC composite presented excellent adsorption performance for multiple cycles.

A comparison of the present work with the reported studies on the adsorption of MB is available in **Table S13**. The removal performance or adsorption capacity of Ce-MOF@Fe_3O_4@AC supersedes many of the reported MOF-based adsorbents. Moreover, some studies have reported high adsorption capacity at a high basic pH value, which is difficult to attain for real wastewater (pH 6.5–7.5). In some studies, the regeneration ability of adsorbent was insufficient for its judicious use in the wastewater treatment facility. Therefore, we have found that the material developed in this study is highly efficient in a wide pH range with exceptional reusability.

4. Conclusion

In this study, we have reported on the fabrication of a magnetic MOF@Fe_3O_4@AC composite for the adsorptive removal of cationic and anionic dyes. FTIR, Raman, XRD, and XPS analysis confirmed the formation of the composite. The composite showed a higher adsorption efficiency compared to its constituents in a wide pH range. The adsorbent showed a ~98–99% dye removal at pH 7, 20 mg dosage, and 3 h of contact time, which was higher than Fe_3O_4@AC (83–85%). The adsorption data for IC and MB fit well with the Temkin and Langmuir isotherm models, respectively. The kinetic data fitted to the Elovich model. The thermodynamics of adsorption confirmed the process to be spontaneous and endothermic with an increase in entropy. Moreover, a slight increase in the adsorption efficiency with temperature suggested the minor influence of chemical forces in the process. The presence of dye in the adsorbent was confirmed by the increased intensity of C—H and C═C bands in the Raman spectra. Moreover, the peak for C—N═C in the HRXPS N 1s spectra confirmed the presence of organic dyes in the spent adsorbent. The involvement of electrostatic and cation-π interactions was confirmed by the shift in the binding energies of Ce and Fe sites. The adsorbent showed 90% removal capacity even after four cycles, making it a suitable adsorbent for the remediation of dye-contaminated wastewater.

Declaration of Competing Interest

The authors declare that they have no known competing financial interests or personal relationships that could have appeared to influence the work reported in this paper.

Acknowledgement

The authors would like to thank Laboratorio Nacional de Ciencia, Tecnología y Gestión Integrada del Agua (LNAGUA) and Laboratorio Nacional de Conversión y Almacenamiento de Energía (LNCAE) for experimental and instrument facilities. Authors would like to thank Grayson Gould, Reliance Canada for language editing. And the support of CONACyT and 20210779 SIP-IPN project.

Authors contribution

Roxana Paz: Material fabrication, adsorption experiments, and manuscript preparation.

Herlys Viltres: Material fabrication and manuscript editing.

Nishesh Kumar Gupta: Manuscript preparation and editing.

Carolina Levya: Conceptualization and manuscript editing.

Appendix A. Supplementary material

Supplementary data to this article can be found online at https://doi.org/10.1016/j.molliq.2021.116578.

References

[1] K. Cendrowski, K. Opała, E. Mijowska, Carbonized lanthanum-based metal-organic framework with parallel arranged channels for azo-dye adsorption, Nanomaterials. 10 (2020), https://doi.org/10.3390/nano10061053.

[2] D. Zhao, C. Cai, Cerium-based UiO-66 metal-organic framework for synergistic dye adsorption and photodegradation: A discussion of the mechanism, Dye. Pigment. 185 (2021), https://doi.org/10.1016/j.dyepig.2020.108957.

[3] M.A. Hassaan, A. El Nemr, Mohamed A. Hassaan, Ahmed El Nemr. Health and Environmental Impacts of Dyes: Mini Review, Am. J. Environ. Sci. Eng. 1 (2017) 64–67, https://doi.org/10.11648/j.ajese.20170103.11.

[4] L.C. Apostol, L. Pereira, R. Pereira, M. Gavrilescu, M.M. Alves, Biological decolorization of xanthene dyes by anaerobic granular biomass, Biodegradation 23 (2012) 725–737, https://doi.org/10.1007/s10532-012-9548-7.

[5] M. Swaminathan, M. Muruganandham, M. Sillanpaa, Advanced oxidation processes for wastewater treatment, Int. J. Photoenergy. 2013 (2013) 85–93, https://doi.org/10.1155/2013/683682.

[6] N.K. Gupta, Y. Ghaffari, S. Kim, J. Bae, K.S. Kim, M. Saifuddin, Photocatalytic Degradation of Organic Pollutants over MFe2O4 (M = Co, Ni, Cu, Zn) Nanoparticles at Neutral pH, Sci. Rep. 10 (2020) 1–11, https://doi.org/10.1038/s41598-020-61930-2.

[7] A. Gupta, H. Viltres, N.K. Gupta, Sono-adsorption of organic dyes onto CoFe2O4/Graphene oxide nanocomposite, Surf. Interfaces 20 (2020), https://doi.org/10.1016/j.surfin.2020.100563 100563.

[8] C. Anushree, J. Philip, Efficient removal of methylene blue dye using cellulose capped Fe 3 O 4 nanofluids prepared using oxidation-precipitation method, Colloids Surf. A Physicochem. Eng. Asp. 567 (2019) 193–204, https://doi.org/10.1016/j.colsurfa.2019.01.057.

[9] P.V. Nidheesh, M. Zhou, M.A. Oturan, An overview on the removal of synthetic dyes from water by electrochemical advanced oxidation processes, Chemosphere 197 (2018) 210–227, https://doi.org/10.1016/j.chemosphere.2017.12.195.

[10] W. Chen, J. Mo, X. Du, Z. Zhang, W. Zhang, Biomimetic dynamic membrane for aquatic dye removal, Water Res. 151 (2019) 243–251, https://doi.org/10.1016/j.watres.2018.11.078.

[11] S. Sangeetha, G. Krishnamurthy, Electrochemical and photocatalytic applications of Ce-MOF, Bull. Mater. Sci. 43 (2020), https://doi.org/10.1007/s12034-020-02225-0.

[12] E. Altintig, M. Onaran, A. Sarı, H. Altundag, M. Tuzen, Preparation, characterization and evaluation of bio-based magnetic activated carbon for effective adsorption of malachite green from aqueous solution, Mater. Chem. Phys. 220 (2018) 313–321, https://doi.org/10.1016/j.matchemphys.2018.05.077.

[13] E. Altıntıg, M. Yenigun, A. Sarı, H. Altundag, M. Tuzen, T.A. Saleh, Facile synthesis of zinc oxide nanoparticles loaded activated carbon as an eco-friendly adsorbent for ultra-removal of malachite green from water, Environ. Technol. Innov. 21 (2021), https://doi.org/10.1016/j.eti.2020.101305.

[14] M. Tuzen, A. Sarı, T.A. Saleh, Response surface optimization, kinetic and thermodynamic studies for effective removal of rhodamine B by magnetic AC/CeO2 nanocomposite, J. Environ. Manage. 206 (2018) 170–177, https://doi.org/10.1016/j.jenvman.2017.10.016.

[15] N. Yang, S. Zhu, D. Zhang, S. Xu, Synthesis and properties of magnetic Fe3O4-activated carbon nanocomposite particles for dye removal, Mater. Lett. 62 (2008) 645–647, https://doi.org/10.1016/j.matlet.2007.06.049.

[16] Y.C. López, G.A. Ortega, E. Reguera, Magnetic detergent with potential application for diesel spills removal from seawater, Colloids Surf. A Physicochem. Eng. Asp. 561 (2019) 120–127, https://doi.org/10.1016/j.colsurfa.2018.10.061.

[17] S. Sun, Q. Yu, M. Li, H. Zhao, C. Wu, Preparation of coffee-shell activated carbon and its application for water vapor adsorption, Renew. Energy. 142 (2019) 11–19, https://doi.org/10.1016/j.renene.2019.04.097.

[18] T.A. Saleh, Simultaneous adsorptive desulfurization of diesel fuel over bimetallic nanoparticles loaded on activated carbon, J. Clean. Prod. 172 (2018) 2123–2132, https://doi.org/10.1016/j.jclepro.2017.11.208.

[19] U.K. Sahu, S. Sahu, S.S. Mahapatra, R.K. Patel, Cigarette soot activated carbon modified with Fe3O4 nanoparticles as an effective adsorbent for As(III) and As(V): Material preparation, characterization and adsorption mechanism study, J. Mol. Liq. 243 (2017) 395–405, https://doi.org/10.1016/j.molliq.2017.08.055.

[20] M. Almáši, V. Zeleňák, M. Opanasenko, I. Císařová, Ce(III) and Lu(III) metal-organic frameworks with Lewis acid metal sites: Preparation, sorption properties and catalytic activity in Knoevenagel condensation, Catal. Today. 243 (2015) 184–194, https://doi.org/10.1016/j.cattod.2014.07.028.

[21] F. Mohammadnezhad, M. Feyzi, S. Zinadini, A novel Ce-MOF/PES mixed matrix membrane; synthesis, characterization and antifouling evaluation, J. Ind. Eng. Chem. 71 (2019) 99–111, https://doi.org/10.1016/j.jiec.2018.09.032.

[22] R. Ramachandran, W. Xuan, C. Zhao, X. Leng, D. Sun, D. Luo, F. Wang, Enhanced electrochemical properties of cerium metal-organic framework based composite electrodes for high-performance supercapacitor application, RSC Adv. 8 (2018) 3462–3469, https://doi.org/10.1039/c7ra12789h.

[23] A. Lazzarini, A. Piovano, R. Pellegrini, G. Agostini, S. Rudić, C. Lamberti, E. Groppo, Graphitization of Activated Carbons: A Molecular-level Investigation by INS, DRIFT, XRD and Raman Techniques, Phys. Procedia, Elsevier B.V. (2016) 20–26, https://doi.org/10.1016/j.phpro.2016.11.076.

[24] M. Testa-Anta, M.A. Ramos-Docampo, M. Comesaña-Hermo, B. Rivas-Murias, V. Salgueiriño, Raman spectroscopy to unravel the magnetic properties of iron oxide nanocrystals for bio-related applications, Nanoscale Adv. 1 (2019) 2086–2103, https://doi.org/10.1039/c9na00064j.

[25] X. Chen, E. Yu, S. Cai, E. Yu, H. Jia, S. Cai, P. Liang, J. Chen, J. Chen, In situ pyrolysis of Ce-MOF to prepare CeO2 catalyst with obviously improved catalytic performance for toluene combustion, Chem. Eng. J. 344 (2018) 469–479, https://doi.org/10.1016/j.cej.2018.03.091.

[26] A. Lin, A.A. Ibrahim, P. Arab, H.M. El-Kaderi, M.S. El-Shall, Palladium Nanoparticles Supported on Ce-Metal-Organic Framework for Efficient CO Oxidation and Low-Temperature CO2 Capture, ACS Appl. Mater. Interfaces. 9 (2017) 17961–17968, https://doi.org/10.1021/acsami.7b03555.

[27] S.C. Rodrigues, M.C. Silva, J.A. Torres, M.L. Bianchi, Use of Magnetic Activated Carbon in a Solid Phase Extraction Procedure for Analysis of 2,4-dichlorophenol in Water Samples, Water. Air. Soil Pollut. 231 (2020), https://doi.org/10.1007/s11270-020-04610-1.

[28] K. Petcharoen, A. Sirivat, Synthesis and characterization of magnetite nanoparticles via the chemical co-precipitation method, Mater. Sci. Eng. B Solid-State Mater. Adv. Technol. 177 (2012) 421–427, https://doi.org/10.1016/j.mseb.2012.01.003.

[29] D. Bhatia, D. Datta, A. Joshi, S. Gupta, Y. Gote, Adsorption Study for the Separation of Isonicotinic Acid from Aqueous Solution Using Activated Carbon/Fe3O4 Composites, J. Chem. Eng. Data. 63 (2018) 436–445, https://doi.org/10.1021/acs.jced.7b00881.

[30] Y. Yao, S. Miao, S. Liu, L.P. Ma, H. Sun, S. Wang, Synthesis, characterization, and adsorption properties of magnetic Fe 3O 4@graphene nanocomposite, Chem. Eng. J. 184 (2012) 326–332, https://doi.org/10.1016/j.cej.2011.12.017.

[31] S.J. Kemp, R.M. Ferguson, A.P. Khandhar, K.M. Krishnan, Monodisperse magnetite nanoparticles with nearly ideal saturation magnetization, RSC Adv. 6 (2016) 77452–77464, https://doi.org/10.1039/c6ra12072e.

[32] A.K. Kar, S.P. Kaur, T.J.D. Kumar, R. Srivastava, Efficient hydrogenolysis of aryl ethers over Ce-MOF supported Pd NPs under mild conditions: mechanistic insight using density functional theoretical calculations, Catal. Sci. Technol. 10 (2020) 6892–6901, https://doi.org/10.1039/d0cy01279c.

[33] S. Zhang, X.Y. Li, J.P. Chen, An XPS study for mechanisms of arsenate adsorption onto a magnetite-doped activated carbon fiber, J. Colloid Interface Sci. 343 (2010) 232–238, https://doi.org/10.1016/j.jcis.2009.11.001.

[34] W. Lu, X. Wu, Ni-MOF nanosheet arrays: Efficient non-noble-metal electrocatalysts for non-enzymatic monosaccharide sensing, New J. Chem. 42 (2018) 3180–3183, https://doi.org/10.1039/c7nj04754a.

[35] A.P. Grosvenor, B.A. Kobe, M.C. Biesinger, N.S. McIntyre, Investigation of multiplet splitting of Fe 2p XPS spectra and bonding in iron compounds, Surf. Interface Anal. 36 (2004) 1564–1574, https://doi.org/10.1002/sia.1984.

[36] N. Zhou, Y. Ma, B. Hu, L. He, S. Wang, Z. Zhang, S. Lu, Construction of Ce-MOF@COF hybrid nanostructure: Label-free aptasensor for the ultrasensitive detection of oxytetracycline residues in aqueous solution environments, Biosens. Bioelectron. 127 (2019) 92–100, https://doi.org/10.1016/j.bios.2018.12.024.

[37] B. Peng, J. Cui, Y. Wang, J. Liu, H. Zheng, L. Jin, X. Zhang, Y. Zhang, Y. Wu, CeO2-:X/C/rGO nanocomposites derived from Ce-MOF and graphene oxide as a

robust platform for highly sensitive uric acid detection, Nanoscale. 10 (2018) 1939–1945, https://doi.org/10.1039/c7nr08858b.

[38] J. He, Y. Xu, W. Wang, B. Hu, Z. Wang, X. Yang, Y. Wang, L. Yang, Ce(III) nanocomposites by partial thermal decomposition of Ce-MOF for effective phosphate adsorption in a wide pH range, Chem. Eng. J. 379 (2020), https://doi.org/10.1016/j.cej.2019.122431.

[39] J. Zheng, Z. Wang, Z. Chen, S. Zuo, Mechanism of CeO2 synthesized by thermal decomposition of Ce-MOF and its performance of benzene catalytic combustion, J. Rare Earths. (2020), https://doi.org/10.1016/j.jre.2020.08.009.

[40] N.K. Gupta, A. Gupta, 2D and 3D carbon-based adsorbents for an efficient removal of HgII ions: A review, FlatChem. 11 (2018) 1–14, https://doi.org/10.1016/j.flatc.2018.11.002.

[41] H. Qiu, L. Lv, B.C. Pan, Q.J. Zhang, W.M. Zhang, Q.X. Zhang, Critical review in adsorption kinetic models, J. Zhejiang Univ. Sci. A. 10 (2009) 716–724, https://doi.org/10.1631/jzus.A0820524.

[42] M. Yang, Q. Bai, Flower-like hierarchical Ni-Zn MOF microspheres: Efficient adsorbents for dye removal, Colloids Surf. A Physicochem. Eng. Asp. 582 (2019), https://doi.org/10.1016/j.colsurfa.2019.123795.

[43] N.K. Gupta, A. Sengupta, A. Gupta, J.R. Sonawane, H. Sahoo, Biosorption-an alternative method for nuclear waste management: A critical review, J. Environ. Chem. Eng. 6 (2018) 2159–2175, https://doi.org/10.1016/j.jece.2018.03.021.

[44] X. Zhao, S. Liu, Z. Tang, H. Niu, Y. Cai, W. Meng, F. Wu, J.P. Giesy, Synthesis of magnetic metal-organic framework (MOF) for efficient removal of organic dyes from water, Sci. Rep. 5 (2015), https://doi.org/10.1038/srep11849.

[45] S. Soni, P.K. Bajpai, J. Mittal, C. Arora, Utilisation of cobalt doped Iron based MOF for enhanced removal and recovery of methylene blue dye from waste water, J. Mol. Liq. 314 (2020), https://doi.org/10.1016/j.molliq.2020.113642.

[46] F. Qiao, J. Wang, S. Ai, L. Li, As a new peroxidase mimetics: The synthesis of selenium doped graphitic carbon nitride nanosheets and applications on colorimetric detection of H2O2 and xanthine, Sensors Actuators, B Chem. 216 (2015) 418–427, https://doi.org/10.1016/j.snb.2015.04.074.

[47] M. Ding, B.H.W.S. De Jong, S.J. Roosendaal, A. Vredenberg, XPS studies on the electronic structure of bonding between solid and solutes: Adsorption of arsenate, chromate, phosphate, Pb2+, and Zn2+ ions on amorphous black ferric oxyhydroxide, Geochim. Cosmochim. Acta. 64 (2000) 1209–1219, https://doi.org/10.1016/S0016-7037(99)00386-5.